

Comparative Investigation of the Downward and Upward Directionally Solidified Single-Crystal Blades of Superalloy CMSX-4



FU WANG, DEXIN MA, SAMUEL BOGNER, and ANDREAS BÜHRIG-POLACZEK

Single-crystal blades of Ni-base superalloys CMSX-4 have been directionally solidified using the downward directional solidification (DWDS) process. The possible benefits of the process were comparatively evaluated with respect to the Bridgman process' results. The DWDS process exhibits good capabilities for casting the single-crystal components. The thermal gradients of this process are approximately seven times higher than those of the Bridgman process. It provides more advantages for solidifying the single-crystal superalloy blades by reducing the casting defects, refining the microstructure, decreasing the size of the γ/γ' eutectic pools, refining the γ' precipitates, alleviating the degree of the microsegregation, and minimizing the size and volume fraction of the micropores.

DOI: 10.1007/s11661-016-3415-9

© The Minerals, Metals & Materials Society and ASM International 2016

I. INTRODUCTION

SINGLE-crystal Ni-based superalloys have found increasing applications for turbine blades and vanes for aero-engines as well as industrial gas turbines (IGTs).^[1–5] The increasing operating temperature requirements for high-efficiency turbines demand that the blades possess increased high-temperature creep and fatigue strengths. The improved high-temperature properties may be achieved *via* development of alloys^[6–11] and the directional solidification (DS) process. Innovations in processing focus on increasing the thermal gradient (G_L) at the solidification front because, during solidification, high thermal gradients assure sequential solidification along the axial direction and prevent equiaxed grains from initiating in constitutional undercooling zones within the melt. The high thermal gradients also reduce segregation and allow the operating temperature of the alloy's components to be increased.^[12]

Since the Bridgman directional solidification process was developed in the 1920s,^[13] a number of directional solidification processes have to date been developed. In the 1970s, a few researchers^[14–16] presented the high-rate solidification (HRS) process based on the Bridgman process in which the concept of mold translation was utilized. HRS can employ various types of radiation baffles to sharpen the thermal gradient between the hot and cool zones of the furnace. Since the original

development of HRS, the process has been highly optimized for the production of aero-engine scale components. However, due to the lower rate of radiative heat exchange, the open baffle insulation between the heating and cooling zones, and the large thermal resistance of the thick ceramic molds (especially for IGTs' blades^[17]), this process results in ineffective heating in the heating zone and inferior heat extraction in the cooling zone. These inefficiencies lead to lower thermal gradients and the occurrence of process problems, such as mold warping and cracking, mold-metal reaction and low yield.^[18] In addition to this, at the beginning of HRS process the heat primarily conducts through the casting to the chill. At increasing distances from the chill, heat extraction thus quickly becomes inefficient owing to the low thermal conductivity of the superalloys. When this occurs, mold radiation to the cooling chamber becomes the dominant method of heat extraction resulting in low thermal gradients ahead of the solidification front.^[19] The experimental results^[20,21] show that the thermal gradients and cooling rates decrease with increasing distance from the chill. Therefore, in order to keep the solid/liquid (S/L) interface stable, the withdrawal rate must be reduced; otherwise casting defects such as stray grains^[2] will occur, which lead to high rejection rates of the castings. Due to the reduction in withdrawal rate, the dwell time of the mold in the heating zone is extended which increases the reaction between the mold and the metal, mold deformation, and the occurrence of cracks.^[22] Some researchers report that using the HRS process for casting clusters, the shadow effect is found.^[23] The mold's shadow side facing the central rod is ineffectively heated, revealing a shadow zone in the center of the cluster. The metallographic examinations demonstrate a high susceptibility to stray grains^[23] and freckles^[24] on the shadow side, while the heater side revealed a conspicuously lower tendency for this phenomenon. The

FU WANG, Scientific Staff, DEXIN MA, Senior Scientist, SAMUEL BOGNER, Ph.D. Student, and ANDREAS BÜHRIG-POLACZEK, Professor, are with the Foundry Institute, RWTH Aachen University, Intzestraße 5, Aachen 52072, Germany. Contact e-mail: darrel0112038@hotmail.com

Manuscript submitted November 12, 2015.

Article published online March 8, 2016

asymmetric thermal conditions cause the asymmetrical formation of these grain defects.

A modified directional solidification process based on the HRS is the liquid-metal cooling (LMC) process. After pouring the melt, the mold is withdrawn from the heating zone to a liquid-metal bath which can effectively extract the heat through convection. In addition to this, a dynamic floating baffle used in this process can effectively insulate the heating and cooling zones of the furnace, which improves the thermal gradient. Previously, much research work was conducted on this process^[25–29] because this process was considered to have great potential for industrial applications to reduce the casting defects occurring in HRS solidified components. The liquid metals used in the LMC process were either Al, Sn, Ga-In alloy, or Ga-In-Sn alloy. In the 1980s, the former Soviet Union originally uses Al as the cooling medium to produce nickel-based superalloy aero-engine parts.^[30,31] Some researchers^[25,27] also use Sn as a coolant to produce IGTs blades. Sn may have more advantages than Al because of its significantly lower melting point. Some researchers report that Ga-In alloy and Ga-In-Sn alloy, which remain liquid at the room temperature, are also used as coolants in the laboratory-scale furnace.^[31–36] These coolants can further enhance the thermal gradient, refine the microstructure, and improve the performance of castings. The LMC process typically produces thermal gradients more than double those achievable with the Bridgman process.^[25] However, this process is also characterized by ineffective radiative heating in the heating zone and large thermal resistance in the thick ceramic molds which limit further improvement in the LMC process' thermal gradient. Moreover, during the LMC process the ceramic mold is subjected to huge thermal impact when immersing into the liquid bath. Mold cracking is very difficult to avoid. This indicates that the liquid-metal coolant will come into contact with the superalloy components. In this case, the casting will be contaminated, and the performance of the castings will be degraded.^[37] The high cost of the coolants and the complex operation of the process also limit its wide application.^[38]

The gas cooling casting (GCC) process was developed at ABB ALSTON Power Technology^[39] for manufacturing large single-crystal components, and provides further improvements upon the LMC. Apart from the radiation cooling, typical for the conventional HRS, the GCC process injects an inert gas directly below the furnace baffle to cool the casting as it is withdrawn from the heating zone. This additional heat extraction due to the convection of the cooling gas not only improves the thermal gradient but also avoids the contamination by the coolants in the LMC process. In addition to this, the cost is greatly reduced compared to that of the LMC process. The thermal heat transfer coefficients of the GCC process are similar to the LMC process.^[39] However, similar to the HRS and the LMC processes, ineffective radiative heating in the heating zone and large thermal resistance due to the thick ceramic molds also exist in this process, and these restrict further enhancement of the thermal gradients of the GCC

process. Moreover, owing to the open baffle insulation between heating and cooling zone in the GCC process, the cooling gas may cool the heating zone. This leads to a reduction in the thermal gradient, and the formation of the stray grains.

The disadvantages stated above limit the wide industrial application of these processes. Recently, the downward directional solidification (DWDS) process was developed.^[40] This process combines the Bridgman process, the GCC process, the dynamic baffle, and the Czochralski process. Here, alloys are overheated to a stable temperature in a crucible and covered with hollow ceramic beads which function as a dynamic baffle. Ceramic molds having single-crystal seeds or a helical selector connected to a chill at one end are inserted into the alloy melt through the dynamic baffle. The other end of the molds is wrapped and sealed by a nickel foil to prevent the entrance of the baffle's beads. When the foil has melted, the alloy melt flows into the molds and comes into contact with the seed or the chill. After a steady-state thermal condition is reached, which is monitored by thermocouples embedded in the seeds or the molds, the molds are withdrawn from the alloy melt at a uniform withdrawal rate and, if necessary, cooled by argon to then form the single-crystal casting. This process permits thin-walled (1 to 2 mm) ceramic molds to be employed since no thermal impact or hydrostatic pressure is exerted by the melt during the pouring process. The molds are much thinner than those used in the above processes (7 to 8 mm). As a consequence, an improved heating and heat extraction efficiency can be achieved which gives rise to an enhanced thermal gradient. Owing to the higher thermal gradient, larger withdrawal rates can be used which can reduce the dwell time of the mold at the high temperature and thus further decrease the reaction between the melt and the mold. Besides this, the castings cannot be contaminated by the coolant because the gas cooling method is employed. However, the pressure of the cooling gas should be controlled to an appropriate value because excessive pressures can cause a transversal diffusion of heat and an occurrence of stray grains. Previous investigations^[40] show that this process exhibits an excellent capability for casting single-crystal blades of pure Al (99.93 pct). In addition to this, our previous research work^[41] demonstrates that this process is also able to cast single-crystal bars of superalloys possessing high monocrystallinity. The G_L in the DWDS solidified superalloy single-crystal bars is 10 to 12 times that of bars solidified in the Bridgman process. The microstructures of these DWDS bars are significantly refined, and the degree of segregation of alloying elements is greatly reduced.^[42] Meanwhile, the freckle defect can be essentially eliminated in the DWDS solidified single-crystal bars of the superalloys.^[43] Indeed, DWDS process has some possible disadvantages such as mold deformation, limitation for the blade size, entering ceramic materials into the melt, and the required mold surface preparation, which will be verified and investigated in our next work.

Previous studies^[44,45] suggest that geometrical features of the castings have a great influence on the

integrity of the single-crystal castings of the superalloys. During the solidification of the single-crystal blades having a complex shape, the liquidus isotherm becomes curved. As a result, an isolated, thermally undercooled region of melt is formed. This may lead to heterogeneous nucleation and the formation of stray grains. In addition to this, considering the low hydrostatic pressure in the DWDS process, the mold filling may become a predominant issue for casting single-crystal blades. Admittedly, an excellent casting capability of the DWDS process is exhibited in casting single-crystal blades of pure Al, but major distinctions exist between pure Al and the superalloys. As a consequence, the investigations reported in this paper have been carried out to study the feasibility of the DWDS process to produce single-crystal blades of the superalloys. The possible benefits of the DWDS process are discussed based on comparisons of the experimental results obtained in the Bridgman process regarding the thermal gradients, the microstructures, the microporosity, and the segregation behavior.

II. EXPERIMENTAL PROCEDURES

A. Materials and Mold Preparation

A second-generation single-crystal superalloy CMSX-4 with a chemical composition of Ni-5.6Al-9.0Co-6.5Cr-0.6Mo-3.0Re-6.5Ta-6.0W (wt pct) was used for this investigation. The ceramic molds used in the DWDS and the Bridgman processes were prepared following the traditional production steps of ceramic molds used in investment casting. For the DWDS solidified mold, since no thermal impact or hydrostatic pressure exerted by the melt during the pouring process, a high strength of the mold is not required and the wall thickness of the mold can be greatly reduced, therefore the investing and stuccoing operations were repeated only three times and the diameter of the sand was 0.12 to 0.25 mm, whereas the traditional operations are repeated 12 times and the diameter of the sand was 0.12 to 1 mm. Following the repetitive operations, the DWDS solidified mold was polished so as to increase the surface smoothness and alleviate the adhesion of the melt on the surface of the mold, and then sealed using the slurry in order to

increase the smoothness of the molds' surfaces. Figure 1 shows the ceramic molds having the blade's shape used in the DWDS and Bridgman processes. It can be clearly seen that the ceramic molds used in the DWDS process (about 1.5 mm in wall thickness) were much thinner than those used in the Bridgman processes (about 8 mm in wall thickness).

B. Casting Single-Crystal Blades Using the DWDS Process

The DWDS experiments were performed using an in-house designed non-vacuum furnace. The casting procedure is schematically depicted in Figure 2. During the experiments, the CMSX-4 superalloy was overheated to 1793 K (1520 °C) in a crucible and covered with hollow Al_2O_3 beads (1 to 3 mm in diameter) acting as a dynamic baffle. Single-crystal seeds of CMSX-4 superalloy with [001] crystal orientation in the longitudinal direction were inserted into one end of the molds, and connected to a water-cooled chill-plate. The other end of the mold was wrapped and sealed using a nickel foil acting as a plug in order to prevent the penetration of the dynamic baffle. The molds were then inserted into the alloy melt. When the foil melted, the alloy melt

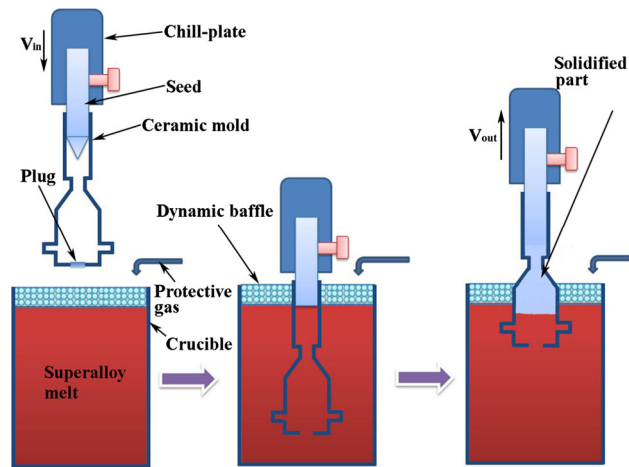


Fig. 2—Schematic description of the DWDS process procedure.

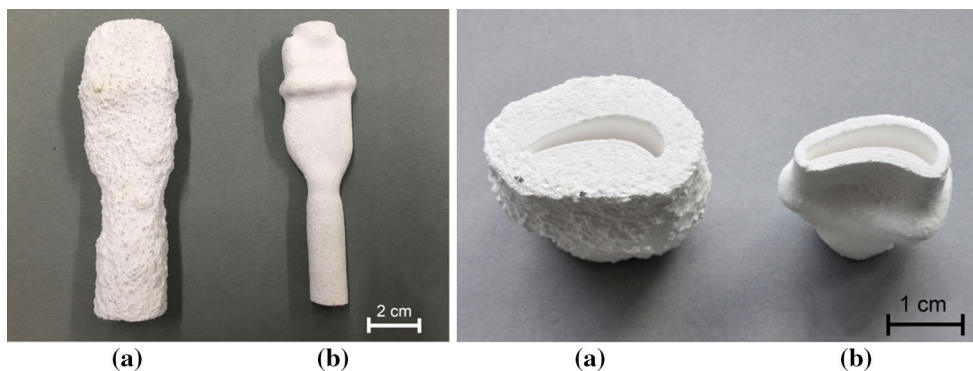


Fig. 1—Ceramic molds used in the (a) Bridgman process and (b) DWDS process.

flowed into the mold and made contact with the seed. Each seed was instrumented with a type-B thermocouple located along its center line. The measurement position in the blades was located 30 mm from the chill. Thermocouple readings were recorded each second during the entire process. When a portion of the seed had melted, the molds were elevated at a withdrawal rate (V) of 2.5 mm min⁻¹ (without argon cooling), and the single-crystal blades were then solidified. During the overheating and withdrawal processes, the alloy melt was protected by Ar gas.

C. Casting Single-Crystal Blades Using the Bridgman Process

For comparison, the Bridgman's blades were solidified using an ALD Vacuum Technologies, Inc. Bridgman furnace. The details of the schematic diagram can be found elsewhere: see Reference 25. During this process, the CMSX-4 superalloy was melted in a crucible which was positioned in the induction melting coil. An investment mold cluster with single-crystal seeds having the same geometry of the components as the DWDS castings was mounted on a water-cooled chill-plate and raised into the mold heater. A vacuum of about 3×10^{-4} mbar was obtained before preheating the mold to a temperature of 1793 K (1520 °C). After equalizing the mold temperature, the melted superalloy was bottom poured into the mold, and the withdrawal sequence was then initiated thus forming the single-crystal castings. Prior to casting, a protective alumina tube, sealed at one end, was embedded in the mold. A type-B thermocouple was inserted into this tube and the cooling curve was recorded during the withdrawal process. The parameters, such as the position of the thermocouple and the withdrawal rates, were identical to those employed in the DWDS process.

D. Microstructure Analysis

After solidification, the blades were then knocked out of the ceramic molds. The blades were then sand blasted to remove any ceramic debris attached to its surface. 80 ml HCl + 20 ml H₂O₂ etchant was employed to examine the macrostructures, and to ascertain the integrity of the single-crystal blades. The blades were then sectioned transversely (perpendicular to the growth direction), and samples were mounted and polished for microstructural analyses. Figure 3 shows the positions of the sectioned DWDS solidified and Bridgman's samples. The transverse sections A of the samples which have a same distance from the bottom of the blades were used to perform the metallographic examination. 60 mL C₂H₅OH + 40 mL HCl + 2g (Cu₂Cl·2H₂O) etchant was used to reveal the microstructures. The microstructural analyses included measurements of the primary dendrite arm spacing (PDAS) (λ_1), the mean areas of the γ'/γ eutectic pools, the average size of the γ' precipitates, and the segregation behavior. The triangle method^[46,47] was used for measuring λ_1 . The triangle is formed by joining the three neighboring dendrite centers, the sides of the triangle corresponding to λ_1 . Using these

methods, 30 values of λ_1 were measured. Three blades are used in the measurements. The mean areas of the eutectic pools were determined by the metallographic analytical software Image-Pro Plus. The size of the γ' phase was determined using $A = (S_T/n)^{1/2}$, where S_T is the cumulative total γ' area of the whole field of view of the micrograph and n is the number of γ' variants. The transverse section of the non-etched samples was photographed using an Axioplan 2 optical microscope (OM) to reveal micropores. Micropore size measurements were obtained using the Image-Pro Plus software. At least 50 micropores were measured in each of the DWDS and the Bridgman solidified blades. The detailed morphologies of the micropores were further characterized using a Zeiss 1540 XB Cross Beam scanning electron microscope (SEM) equipped with an energy-dispersive spectroscopy (EDS) system. The segregation behavior of alloying elements was also examined using this device. Ten dendrites and interdendritic regions were investigated. Three points in the dendrite core and the interdendritic regions were examined, and the average values of the contents of the alloying elements were used to calculate the segregation coefficient (k').

III. RESULTS AND DISCUSSION

A. Thermal Gradients at the Solidification Front (G_L)

Figure 4 shows the cooling curves measured during the solidification of the DWDS and Bridgman solidified single-crystal blades. To obtain the thermal gradient at the solidification front (G_L), the cooling rate (\dot{T}) was first calculated from the cooling curve's slope at the liquidus temperature. The thermal gradient was then calculated by dividing the cooling rate by the withdrawal rate (V): $G_L = \dot{T}/V$. The calculated thermal gradient in the DWDS process was 14.16 K (14.16 °C) mm⁻¹, while that in the Bridgman process was 2.16 K (2.16 °C) mm⁻¹. The thermal gradient in the DWDS process is approximately 6.56 times higher than that in the Bridgman process.

Previous studies^[48] showed that a higher thermal gradient (G_L) in a cylindrical rod can be functionally expressed according to Eq. [1]:

$$G_L = [2h(T_s - T_0)a/Vr - \rho_s LV]/k_L, \quad [1]$$

where ρ_s is the density; k_L is the liquid thermal conductivity; V is the crystal growth velocity (supposing that V is equal to withdrawal rate); r is the radius of the cylindrical rod casting; T_s and T_0 are the temperatures of the solid casting and the cooling medium, respectively; h is the combined coefficient of heat transfer; L is the latent heat; and a is the heat diffusivity.

Since, in this experiment, a low withdrawal rate was employed, the second term on the right-hand side of Eq. [1] can be neglected. The ratio between the thermal gradient ($G_{L(DWDS)}$) in the DWDS process and that ($G_{L(Bridgman)}$) in the Bridgman process can be expressed as

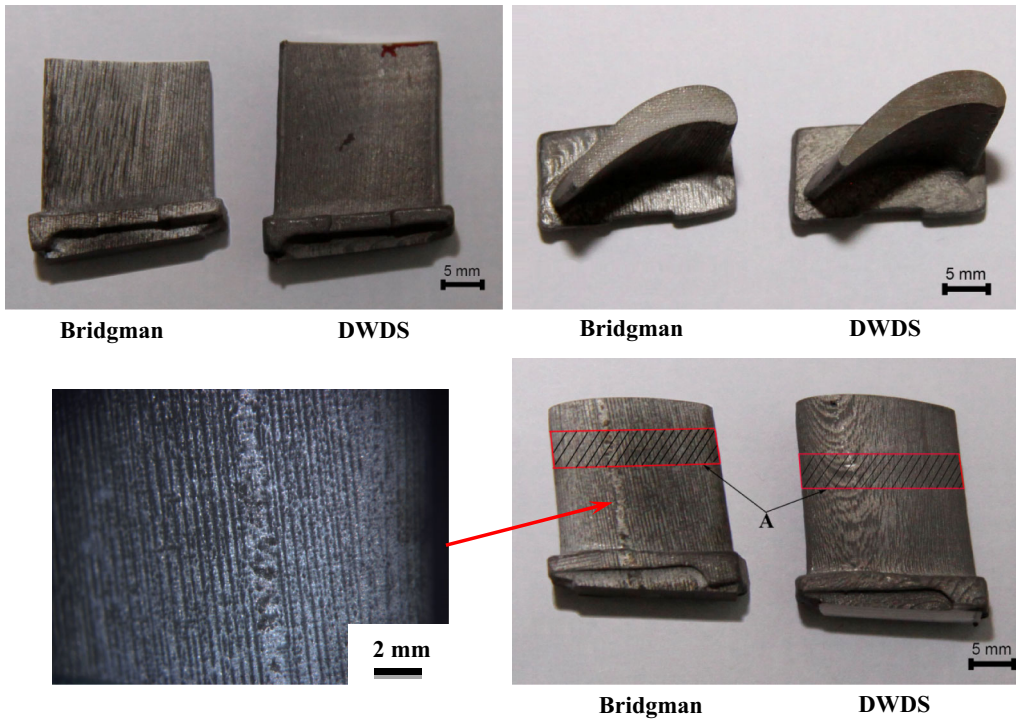


Fig. 3—DWDS and Bridgman processes of single-crystal blades solidified and macro-etched, and the sectioned position of the metallographic samples (red rectangle) (Color figure online).

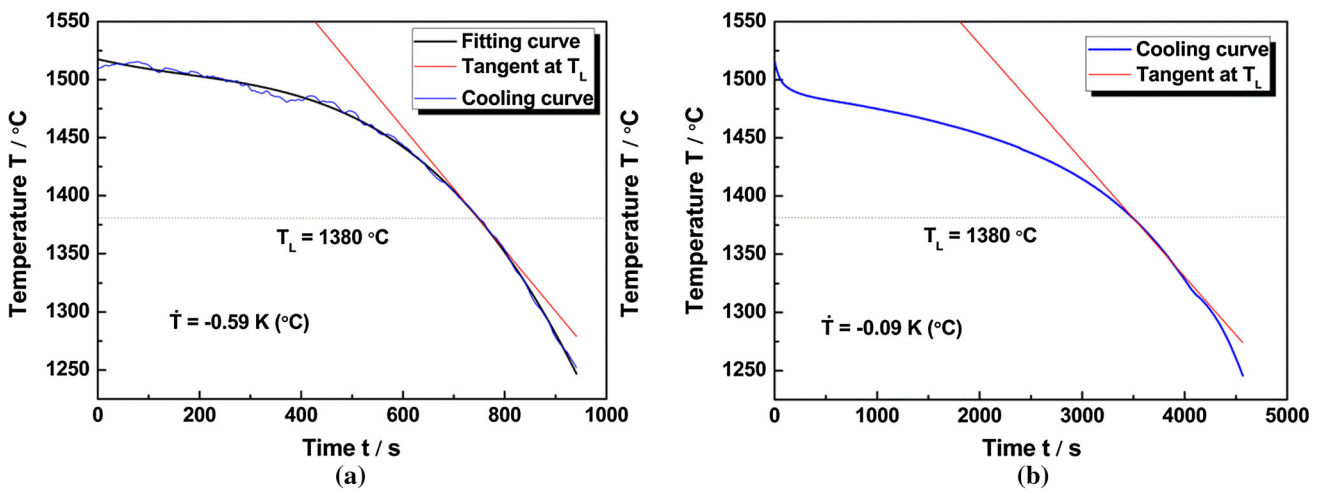


Fig. 4—Cooling curves and cooling rates measured in the (a) DWDS and (b) Bridgman solidified blades during the solidification.

$$G_{L(DWDS)}/G_{L(Brigman)} = h_{DWDS}/h_{Bridgman}. \quad [2]$$

Assuming that the conduction through the ceramic mold to the mold's outer surface is the heat transfer limiting step, and the other steps are negligible, the combined heat transfer coefficients (h_{DWDS} and $h_{Bridgman}$) of the DWDS and Bridgman casting systems are then equal to the conductive heat transfer coefficients (h_{mold}). These coefficients can be calculated by λ_{mold}/l , where λ_{mold} is the thermal conductivity and l is the wall thickness of the molds. As a consequence, Eq. [2] can be expressed as

$$G_{L(DWDS)}/G_{L(Brigman)} = l_{Bridgman}/l_{DWDS}. \quad [3]$$

In terms of Eq. [3], the thermal gradient in the DWDS process can be approximately evaluated as 5.3 times larger than that in the Bridgman process. Previous investigation suggests that the baffle geometry has a strong effect on the thermal gradient.^[49] In comparison to the baffle in the Bridgman process, the dynamic baffle used in the DWDS process can perfectly shield from the heat, and further increases the thermal gradient. If the effects of the improved thermal insulation of the dynamical baffle are considered, the thermal gradient

in the DWDS process is almost equal to the measured values. This, in turn, is good evidence that the assumptions made above are reasonable.

B. Macrostructure

Figure 3 shows the macro-etched surface characteristics exhibited by the blades solidified using DWDS and Bridgman processes. It depicts typical features of the single-crystal blade surfaces with clear traces of [001] oriented dendrites. Typical freckle defects, arising due to density inversions and exhibiting a small chain of equiaxed grains aligned approximately parallel to the solidification directions, were found on the surfaces of the Bridgman solidified blades but not visible on the surfaces of the DWDS solidified blades. No other defects, such as stray grains, silvers, and high-angle boundaries, were observed on the solidified blade surfaces of either process.

C. Microstructures

1. Primary dendrite arm spacing (λ_1)

Images of transverse sections of the DWDS and Bridgman solidified blades are illustrated in Figures 5(a) and (b). Enlarged images which were chosen from the thickest blade sections are shown in Figures 5(c) and (d). A substantial refinement in the primary dendrite is observed in the DWDS blades. In order to quantitatively assess the degree of the refinement, the primary dendrite arm spacings at the thickest section were measured and averaged. The average λ_1 is shown in Figure 6. The measured average λ_1 of the DWDS solidified blades was 299.28 μm , while the average is almost 445.61 μm in the Bridgman blades. A reduction of 146 μm in λ_1 was observed in the DWDS solidified blades. Although the thermal gradient of the DWDS process is 6.5 times higher than that in the Bridgman

process, the λ_1 does not significantly change. The reason for this is that λ_1 is not a monotone decreasing function with increasing thermal gradient.^[50]

Previous studies^[51] reported that the primary dendrite arm spacing is inversely proportional to the square root of thermal gradient at the solidification front. The DWDS process produces higher thermal gradients than those in the Bridgman process. These higher thermal gradients can significantly refine the primary dendrites and reduce the primary dendrite arm spacing. Therefore, the DWDS blades have finer primary dendrites and λ_1 is smaller than that for Bridgman blades (Figures 5 and 6).

2. γ/γ' eutectic in the interdendritic regions

γ/γ' eutectic is a non-equilibrium microstructure which forms during the final stage of the solidification process and is detrimental to the performance of the resulting components. For this reason, this eutectic must

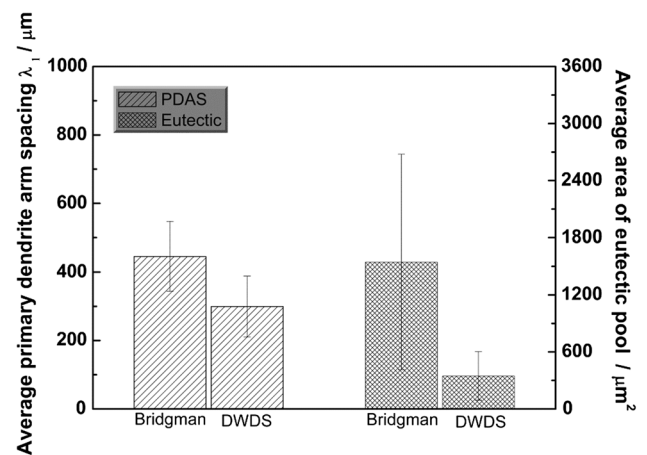


Fig. 6—Average λ_1 and area of the γ/γ' eutectic pools of the DWDS and Bridgman solidified single-crystal blades.

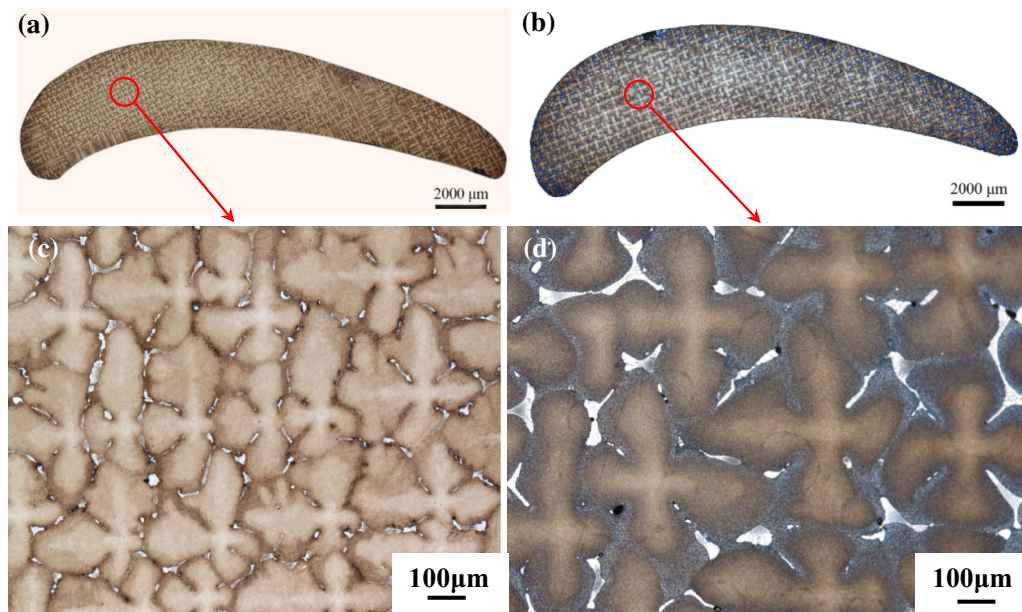


Fig. 5—Images of transverse sections and the enlarged thickest regions of (a, c) the DWDS and (b, d) the Bridgman solidified blades.

be dissolved by the subsequent heat treatment (solution treatment) process. The size of the eutectic pool determines the time of the solution treatment process, and further influences the cost of the heat treatment. Typical morphologies of the γ/γ' eutectic in the blades solidified using the two processes are shown in Figure 7. A large block-like γ/γ' eutectic pool is found in the blades cast by the Bridgman process, whereas a small pool is revealed in the DWDS solidified blades. The average sizes of the γ/γ' eutectic pools were measured and are shown in Figure 6. A decrease of about $1198 \mu\text{m}^2$ in the pool area is observed in the DWDS cast blades. In addition to this, the area fractions of the eutectic pools were also measured. They are 3.45 pct for the DWDS process and 4.59 pct for the Bridgman process. A reduction of 1.14 pct in the area fraction is found in the DWDS solidified blades.

During the final stage of the solidification, the residual liquids in the interdendritic regions are divided into a number of liquid pools and, because they impinge on the dendrites, are enclosed by the dendrite arms. As the solidification proceeds, the γ'/γ eutectic-forming elements (Al, Ti, and Ta) are significantly enriched in the liquid pools. When the concentrations of these elements reach the eutectic reaction point, the γ'/γ eutectic transformation occurs. Higher thermal gradients result in a higher solidification rate (the cooling rate) which greatly reduces the primary and secondary dendrite arm spacings, and thus further decreases the sizes of the isolated liquid pools. As a consequence of this, the DWDS solidified blades have smaller γ'/γ eutectic pools than those solidified using the Bridgman process, as shown in Figure 7. On the other hand, higher thermal gradient can improve the homogeneity of the distribution of alloying elements (shown in Figure 11(b)), which reduces the area fraction of the eutectic pools. Therefore, in comparison to the Bridgman solidified blades, the DWDS cast blades have smaller area fraction of the eutectic pools.

3. γ' precipitates

γ' precipitates are a major strengthening phase in the Ni-based superalloy. These coherently precipitate from the γ matrix by solid-state transformation. Figure 8

shows the metallographic images of the γ' precipitates in the dendrite core and interdendritic regions for the DWDS and the Bridgman solidified blades. Based on these images, the average diameters of the γ' precipitates were measured, and the averages are shown in Figure 9. These results reveal that the size of the γ' precipitates is smaller in the dendrite core than that in the interdendritic regions. In comparison to the Bridgman process, the γ' precipitates are significantly refined. The average diameters of these phases in the dendrite core and interdendritic regions are 49.9 and 30.2 pct, respectively, smaller than those in the Bridgman cast blades.

The size of the γ' phase is influenced by the nucleation and growth conditions. The driving forces for the nucleation of the γ' phase are the degrees of supercooling and supersaturation. At constant withdrawal rate, the higher cooling rates caused by the higher thermal gradient result in an increase in the degree of supercooling, and thus not only promote the nucleation rate of the γ' phase but also reduce the phase's growing time. As a consequence, a more refined γ' phase was found in the DWDS solidified blades. Previous study indicates that the equilibrium partition coefficients of the γ' -forming elements Al and Ta are smaller than one.^[52] It suggests that during the solidification, Al and Ta are enriched in the interdendritic regions. At temperature close to the solidus, the γ phase in these regions dissolves relatively larger amounts of Al and Ta than that in the dendrite core. On decreasing temperature, the γ phase in the interdendritic regions achieves a larger supersaturation than that in the dendrite core, which enhances the growth kinetics and velocity for the γ' phase.^[53] For this reason, the size of the γ' phase in the interdendritic regions is larger than that in the dendrite cores, as shown in Figures 8 and 9.

4. Microporosity

Microporosity is a critical defect of the as-cast single-crystal Ni-based superalloys, and occurs by the shrinkage during the final stage of solidification. Figure 10 depicts micropores within the transverse sections of the DWDS and Bridgman solidified blades. Figure 9 illustrates the volume fractions of the micropores measured in the metallographic sections.

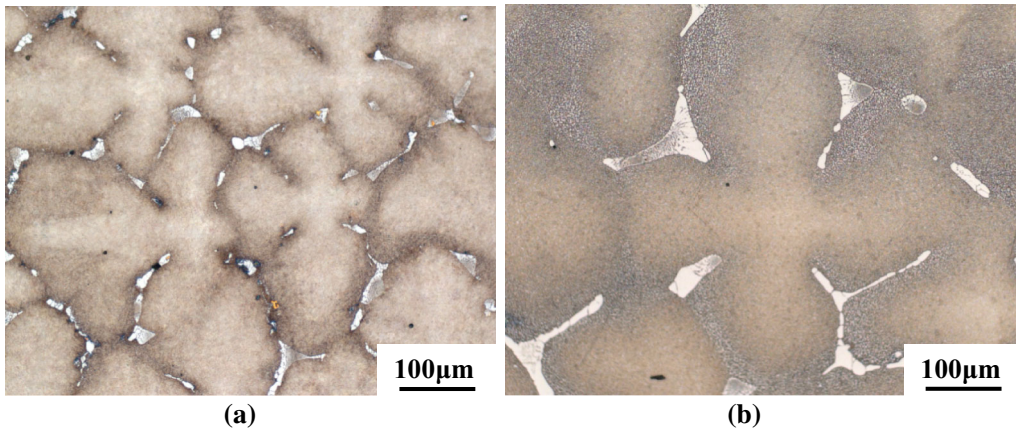


Fig. 7—Morphologies of the γ/γ' eutectic in (a) the DWDS and (b) Bridgman solidified blades.

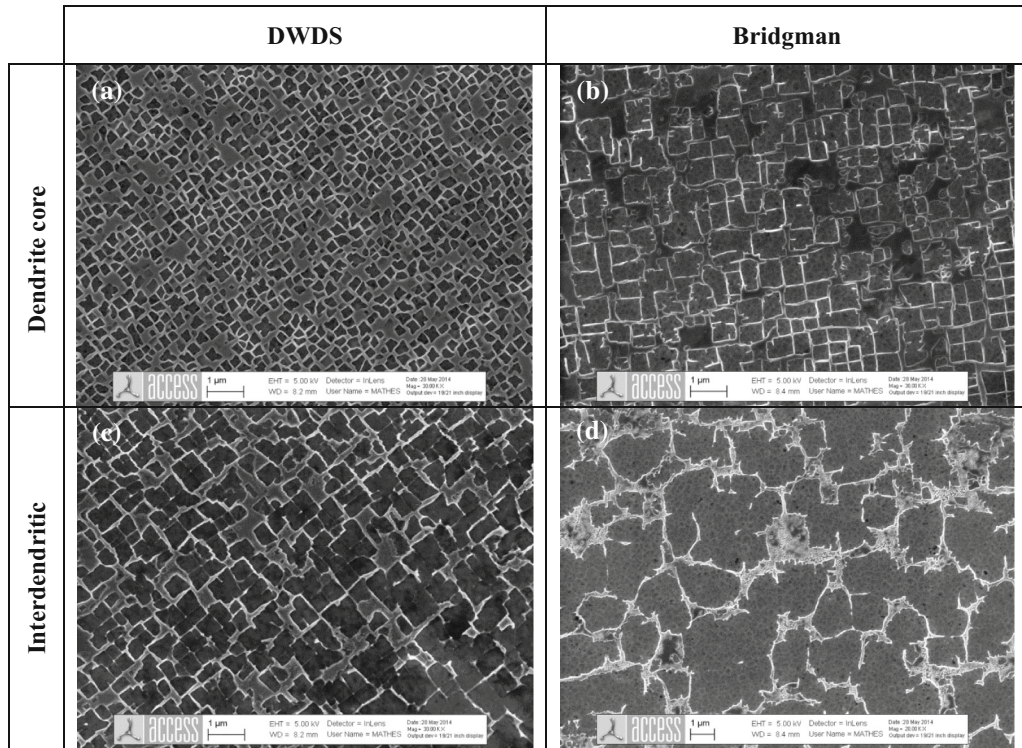


Fig. 8—Typical morphology of the γ' precipitates in (a, b) the dendrite core and (c, d) interdendritic regions of (a, c) the DWDS and (b, d) Bridgman cast single-crystal CMSX-4 blades.

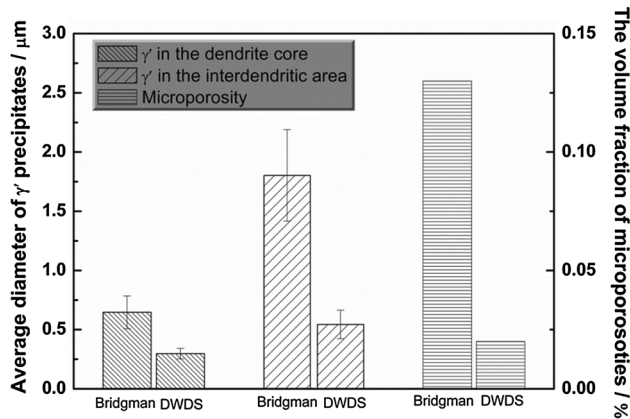


Fig. 9—Average diameters of the γ' precipitates in the dendrite core and interdendritic regions, as well as the volume fraction of the microporosities in the DWDS and Bridgman cast blades.

Differences in the volume fractions and size of the micropores can be found in Figures 9 and 10, respectively. In contrast to the Bridgman blades, both the size and the volume fraction of the micropores are reduced. The volume fractions of the micropores are 0.13 and 0.02 pct in the Bridgman and DWDS solidified blades, respectively. This indicates that using the DWDS process, the microporosity can be effectively reduced.

Hydrostatic pressure due to the bulk liquid contributes to the feeding (mass feeding) during the solidification. In comparison to the Bridgman process, the hydrostatic pressure is low during the DWDS process. However, some researchers reported^[54] that

mass feeding due to the hydrostatic pressure ceases when about 70 pct of the alloy has solidified. Previous studies^[55–59] also reported that the extent of the microporosity is directly related to the thermal gradient, and that an increase in thermal gradient decreases the volume fraction and size of the micropores. Higher thermal gradients in the DWDS process significantly reduce the dendrite arm spacings, and these smaller spacings can decrease the amount of the residual liquid enclosed by the impingement of dendrites in the interdendritic regions. During the solidification, shrinkage is low and the size of the micropores is reduced. In addition to this, the interdendritic feeding path (mushy zone) can be significantly shortened under higher thermal gradients. The shortened mushy zone also further improves the feeding capability. Apart from this, Campbell^[60] suggests that at other times, what appears to be shrinkage porosity is most often not shrinkage at all but is a mass of oxides generated by the entrainment of the oxide bifilms in the turbulence of the alloy melt's pouring. In the Bridgman process, the alloy melt is poured from a furnace and travels through a funnel and a series of channels before entering the casting. The defects from previous pouring events will be inherited. The pores can form from the entrained defects. However, the DWDS process does not involve pouring of the alloy melt. In other words, the DWDS process is reasonably free from oxide bifilms, and the volume fraction of micropores is therefore decreased. Based on the reasons outlined above, a huge reduction in microporosity was observed in the DWDS process.

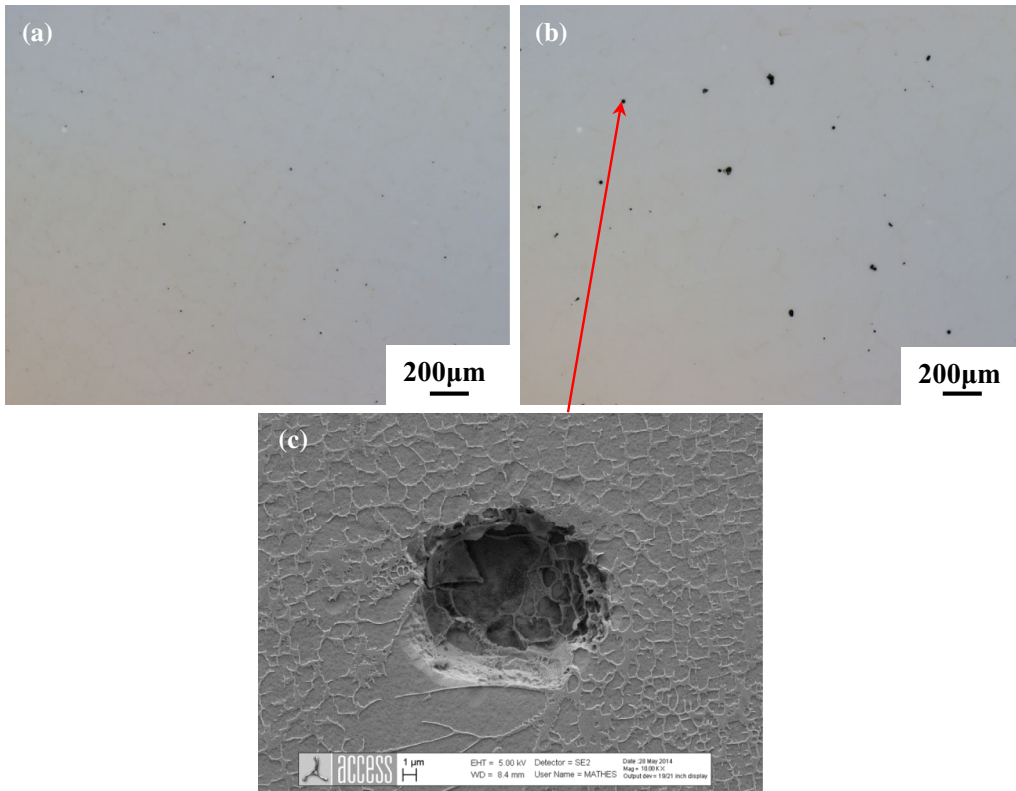


Fig. 10—Micrographs of transverse sections of the DWDS and the Bridgman solidified blades. Microporosity is shown as dark voids for (a) the DWDS and (b) Bridgman solidified blades. An image of a micropore taken using scanning electron microscopy (SEM) is shown in (c).

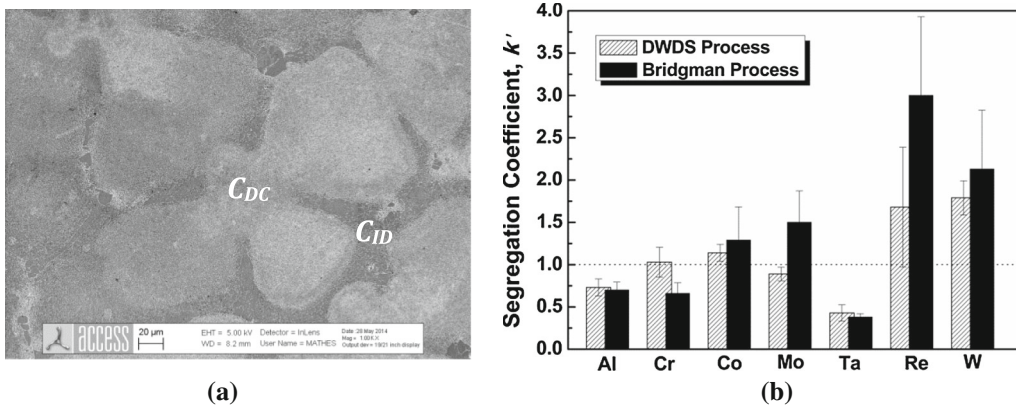


Fig. 11—The examined positions of the alloying elements' concentrations in the cross sections of the blades (a) (C_{DC} and C_{ID} are the concentrations of an alloying element in the center of dendrite core and in the interdendritic regions, respectively) and the calculated segregation coefficients (b).

5. Microsegregation

A parameter used to characterize the segregation behavior is the segregation coefficient (k') which can be expressed as C_{DC}/C_{ID} , where C_{DC} and C_{ID} are the concentrations of an alloying element (wt pct) in the center of dendrite cores and in the interdendritic regions, respectively. When the value of an alloying element's coefficient is less than one, it indicates that this element segregates to the interdendritic regions and is a positive element; otherwise it segregates in the dendrite core and is a negative element. The more the coefficient value

deviates from one, the more severe the alloying element's degree of segregation.

Figure 11(a) shows the examined positions of the alloying elements' concentrations. The calculated segregation coefficients are illustrated in Figure 11(b). From these figures, one can obtain that Al and Ta are the positive segregation elements, whereas Re, W, and Co are the negative elements. Cr and Mo have no strong tendency to segregate to either the dendrite core or the interdendritic regions. In addition to this, the segregation coefficients of the respective alloying elements in the

DWDS solidified blades are closer to one than those in the Bridgman process. This indicates that the alloying elements' degrees of segregation are weaker in the DWDS cast blades.

A large thermal gradient leads to a high cooling rate. Subjected to this high cooling rate, the local solidification time ($\Delta T/G_L V$, where ΔT is the solidification interval) is significantly reduced. The solutes built up ahead of the solidification front have insufficient time to preferentially diffuse to the remote locations in the liquid (the partition coefficient (k) of the elements <1) or in the solidified metal (the partition coefficient (k) of the elements >1) by the homogeneous back-diffusion. These solutes will be entrapped by the solidification front and solidified in situ rendering microsegregation less pronounced in the final stage of the solidification.^[61] As a consequence, the segregation coefficients of the alloying elements in the DWDS solidified blades are closer to one (shown in Figure 11(b)), and the degree of the microsegregation of these elements is thus reduced.

D. Casting Defects

During the solidification of single-crystal superalloy blades, two types of the macro-casting defects, stray grains and freckles, are frequently found. The occurrence of these defects not only depends on the composition of the alloy, but also on the casting conditions. In comparison to the Bridgman process, the DWDS process can essentially eliminate the freckles.^[43] Apart from this, the higher thermal gradient of the DWDS process can keep a straight liquid and solid (L/S) interface, which can effectively reduce the occurrence of the stray grains, especially in the shroud of the blades. However, in terms of the characteristics of the DWDS process the ceramic mold materials may be entered into the melt, and form the inclusions, which need to be further investigated in the future work.

IV. CONCLUSIONS

Using the downward directional solidification (DWDS) process, single-crystal blades having a complex geometric shape were solidified. The possible benefits of this process were evaluated based on comparative results for the Bridgman process. The DWDS process demonstrates good capabilities for casting the single-crystal superalloy blades. This process generates thermal gradients which are approximately seven times that of the Bridgman process. Moreover, the process provides more advantages for solidifying the single-crystal superalloy blades by refining their microstructures, reducing casting defects, and alleviating the degree of the microsegregation.

ACKNOWLEDGMENTS

This research was supported by the Deutsche Forschungsgemeinschaft under Grant No. MA 2505/

3-1. The authors would like to acknowledge the aid of Elke Schabberger-Zimmermann, Elke Breuer, and Maria Schaarschmidt.

REFERENCES

1. T.M. Pollock: *J. Propul. Power*, 2006, vol. 22, pp. 361–74.
2. N. D'souza, M.G. Ardakani, M. Mclean, and B.A. Shollock: *Metall. Mater. Trans. A*, 2000, vol. 31A, pp. 2877–86.
3. M.L. Clemens, A. Price, and R.S. Bellows: *JOM*, 2003, vol. 55, pp. 27–31.
4. X.B. Zhao, L. Liu, C.B. Yang, Y.F. Li, J. Zhang, Y.L. Li, and H.Z. Fu: *J. Alloy. Compd.*, 2011, vol. 509, pp. 9645–49.
5. N. D'souza, M.G. Ardakani, A. Wagner, B.A. Shollock, and M. Mclean: *J. Mater. Sci.*, 2002, vol. 37, pp. 481–87.
6. D. Blavette, P. Caron, and T. Khan: *Scripta Metall.*, 1986, vol. 20, pp. 1395–1400.
7. J.R. Li, D.Z. Tang, R.L. Lao, S.Z. Liu, and Z.T. Wu: *J. Mater. Sci. Technol.*, 1999, vol. 15, pp. 53–57.
8. A.C. Yeh and S. Tin: *Scripta Mater.*, 2005, vol. 52, pp. 519–24.
9. A. Heckl, S. Neumeier, M. Göken, and R.F. Singer: *Mater. Sci. Eng. A*, 2011, vol. 528, pp. 3435–44.
10. A.F. Giamei and D.L. Anton: *Metall. Trans. A*, 1985, vol. 16, pp. 1997–2005.
11. S. Neumeier, F. Pyczak, and M. Göken: in *Superalloys 2008*, R.C. Reed, K.A. Green, P. Caron, T.P. Gabb, M.G. Fahrman, E.S. Huron, and S.A. Woodard, eds., TMS, Warrendale, PA, 2008, pp. 109–19.
12. C.L. Brundidge, J.D. Miller, and T.M. Pollock: *Metall. Mater. Trans. A*, 2011, vol. 42A, pp. 2723–32.
13. P.W. Bridgman: US Patent 1,793,672, 1931.
14. E.G. Laux and S.C. Tingquist: U.S. Patent 3,841,384, 1974.
15. M. Gell, C.P. Sullivan, and F.L. Versnyder: in *Solidification technology*, J.J. Burke, M.C. Flemings, and A.E. Gorum, eds., Brook Hill Pub., MA, 1974, pp. 141–64.
16. J.S. Erickson, W.A. Owczarski, and P.W. Curran: *Metal Progress*, 1971, vol. 99, pp. 58–60.
17. B.B. Seth: in *Superalloys 2000*, T.M. Pollock, R.D. Kissinger, R.R. Bowman, K.A. Green, M. McLean, S.L. Olson, and J.J. Schirra, eds., TMS, Warrendale, PA, 2000, pp. 3–16.
18. R.F. Singer: in *Materials for advanced power engineering*, D. Coutsouradis, J.H. Davidon, J. Ewald, P. Greenfield, T. Khan, M. Malik, D.B. Meadowcroft, V. Regis, R.B. Scarlin, F. Schubert, and D.V. Thornton, eds., Kluwer Academic Publishers Group, Dordrecht, 1994, pp. 1707–29.
19. A. Kermanpur, M. Rappaz, N. Varahram, and P. Davami: *Metall. Mater. Trans. B*, 2000, vol. 31B, pp. 1293–1304.
20. P. Carter, D. Cox, C.A. Gandin, and R. Reed: in *Solidification and casting*, B. Cantor and K. O'Reilly, eds., Institute of Physics Publishing, London, 2003, pp. 106–20.
21. P. Carter, D.C. Cox, C.A. Gandin, and R. Reed: *Mater. Sci. Eng. A*, 2000, vol. 280, pp. 233–46.
22. T.J. Fithgerald and R.F. Singer: *Metall. Mater. Trans. A*, 1997, vol. 28A, pp. 1377–83.
23. D.X. Ma, Q. Wu, S. Hollad, and A. Bührig-Polaczek: *IOP Conf. Ser.: Mater. Sci. Eng.*, 2011, vol. 27, p. 012037.
24. D.X. Ma, Q. Wu, and A. Bührig-Polaczek: *Metall. Mater. Trans. B*, 2012, vol. 43B, pp. 344–53.
25. A.J. Elliott, T.M. Pollock, S. Tin, W.T. King, S.-C. Huang, and M.F.X. Gigliotti: *Metall. Mater. Trans. A*, 2004, vol. 35A, pp. 3221–31.
26. J.G. Tschinkel, A.F. Giamei, and B.H. Kearns: U.S. Patent 3,763,926, 1973.
27. A.F. Giamei and J.G. Tschinkel: *Metall. Trans. A*, 1976, vol. 7A, pp. 1427–34.
28. A.J. Elliott: *Directional Solidification of Large Cross-Section Ni-Base Superalloy Castings via Liquid-Metal Cooling*, The University of Michigan, 2005.
29. L. Liu, T.W. Huang, M. Qu, G. Liu, J. Zhang, and H.Z. Fu: *J. Mater. Process. Technol.*, 2010, vol. 210, pp. 159–65.
30. V.V. Gerasimov: U.S.S.R. Patent 2,836,278/22-02, 1981.
31. R.E. Shalin and V.A. Pankratov: *Metall. Sci. Technol.*, 1992, vol. 10, pp. 3–9.

32. S.F. Gao, L. Liu, N. Wang, X.B. Zhao, J. Zhang, and H.Z. Fu: *Metall. Mater. Trans. A*, 2012, vol. 43A, pp. 3767–75.
33. G. Liu, L. Liu, C. Ai, B.M. Ge, J. Zhang, and H.Z. Fu: *J. Alloy. Compd.*, 2011, vol. 509, pp. 5866–72.
34. X.B. Zhao, L. Liu, Z.H. Yu, W.G. Zhang, and H.Z. Fu: *Mater. Character.*, 2010, vol. 61, pp. 7–12.
35. B.M. Ge, L. Liu, J. Zhang, Y.F. Li, H.Z. Fu, and X.F. Liu: *China Foundry*, 2013, vol. 10, pp. 24–30.
36. J. Wang, Z.M. Ren, Y. Fautrelle, X. Li, H. Nguyen-Thi, N. Mangelinck-Noel, G.S.A. Jaoude, Y.B. Zhong, I. Kaldre, and A. Bojarevics: *J. Mater. Sci.*, 2013, vol. 48, pp. 213–19.
37. J. Zhang and L.H. Luo: *J. Mater. Sci. Technol.*, 2007, vol. 23, pp. 289–300.
38. A. Lohmüller, W. Eßer, J. Großmann, M. Hördler, J. Preuhs, and R.F. Singer: in *Superalloys 2000*, T.M. Pollock, R.D. Kissinger, R.R. Bowman, K.A. Green, M. McLean, S.L. Olson, and J.J. Schirra, eds., TMS, Warrendale, PA, 2000, pp. 181–88.
39. M. Konter, E. Kats, and N. Hofmann: in *Superalloys 2000*, T.M. Pollock, R.D. Kissinger, R.R. Bowman, K.A. Green, M. McLean, S.L. Olson, and J.J. Schirra, eds., TMS, Warrendale, PA, 2000, pp. 189–200.
40. D.X. Ma, H. Lu, and A. Bührig-Polaczek: *IOP Conf. Ser.: Mater. Sci. Eng.*, 2011, vol. 27, p. 012036.
41. F. Wang, D.X. Ma, J. Zhang, S. Bogner, and A. Bührig-Polaczek: *J. Mater. Process. Technol.*, 2014, vol. 214, pp. 3112–21.
42. F. Wang, D.X. Ma, J. Zhang, L. Liu, J. Hong, S. Bogner, and A. Bührig-Polaczek: *J. Alloy. Compd.*, 2015, vol. 647, pp. 528–32.
43. F. Wang, D.X. Ma, J. Zhang, and A. Bührig-Polaczek: *J. Alloy. Compd.*, 2015, vol. 620, pp. 24–30.
44. D.X. Ma and A. Bührig-Polaczek: *Int. J. Cast Metal. Res.*, 2009, vol. 22, pp. 422–29.
45. M. Meyer ter Vehn, D. Dedecke, U. Paul, and P.R. Sahn: in *Superalloys 1996*, R.D. Kissinger, D.J. Deye, D.L. Anton, A.D. Cetel, M.V. Nathal, T.M. Pollock, and D.A. Woodford, eds., TMS, Warrendale, PA, 1996, pp. 471–79.
46. M. Gündüz and E. Cadirli: *Mater. Sci. Eng. A*, 2002, vol. 327, pp. 167–85.
47. O.L. Rocha, C.A. Siqueira, and A. Garcia: *Metall. Mater. Trans. A*, 2003, vol. 34A, pp. 995–1006.
48. H.Z. Fu, J.J. Guo, L. Liu, and J.S. Li: *Directional Solidification and Processing of Advanced Materials*, 1st ed., China Science Publishing & Media Ltd, Beijing, 2006, p. 498.
49. M.M. Franke, R.M. Hilbinger, A. Lohmüller, and R.F. Singer: *J. Mater. Process. Technol.*, 2013, vol. 213, pp. 2081–88.
50. W. Kurz and D.J. Fisher: *Fundamentals of solidification*, 4th rev. ed., p. 83, Trans Tech Publication Ltd, Uetikon-Zuerich, 1998.
51. R. Trivedi: *Metall. Trans. A*, 1984, vol. 15, pp. 977–82.
52. D. Ma and U. Grafe: *Int. J. Cast Metals Res.*, 2000, vol. 13, pp. 85–92.
53. J.M. Xiao: *Alloys and Phases Transition*, 2nd rev. ed., p. 302, Metallurgical Industry Press, Beijing, 2004.
54. K.O. Yu, M.J. Boffel, M. Robinson, D.D. Goettsch, B.G. Thomas, D. Pinella, and R.G. Carlson: *AFS Trans*, 1990, vol. 98, pp. 417–28.
55. J. Lecomte-Beckers: in *Superalloys 1988*, S. Reichman, D.N. Duhl, G. Maurer, S. Antolovich, and C. Lund, eds., TMS, Warrendale, PA, 1988, pp. 713–21.
56. J. Lecomte-Beckers: *Metall. Trans. A*, 1988, vol. 19, pp. 2341–48.
57. D.R. Poirier, K. Yeum, and A.L. Maples: *Metall. Trans. A*, 1987, vol. 18, pp. 1979–87.
58. J. Zhang, J.G. Li, T. Jin, X.F. Sun, and Z.Q. Hu: *J. Mater. Sci. Technol.*, 2010, vol. 26, pp. 889–94.
59. S.M. Seo, J.H. Lee, Y.S. Yoo, C.Y. Jo, H. Miyahara, and K. Ogi: *Metall. Mater. Trans. A*, 2011, vol. 42A, pp. 3150–59.
60. J. Campbell: *Complete Casting Handbook: Metal Casting Processes, Metallurgy, Techniques and Design*, 1st ed., Elsevier, Oxford, 2011, p. 391.
61. W. Kurz and D.J. Fisher: *Fundamentals of solidification*, 4th rev. ed., p. 85, Trans Tech Publication Ltd, Uetikon-Zuerich, 1998.